JOURNAL OF PETROLOGY | VOLUME 45 | NUMBER 12 | PAGES 2369–2388 | 2004 | doi:10.1093/petrology/egh042

The Liquid Line of Descent of Anhydrous, Mantle-Derived, Tholeiitic Liquids by Fractional and Equilibrium Crystallization—an Experimental Study at 1·0 GPa

SAMUEL VILLIGER[1]*, PETER ULMER[1], OTHMAR MÜNTENER[2]† AND ALAN BRUCE THOMPSON[1]

[1]DEPARTMENT OF EARTH SCIENCES, ETH ZURICH, SONNEGGSTRASSE 5, 8092 ZURICH, SWITZERLAND

[2]INSTITUTE OF GEOLOGY, UNIVERSITY OF NEUCHÂTEL, RUE EMILE-ARGAND 11, 2007 NEUCHÂTEL, SWITZERLAND

RECEIVED SEPTEMBER 1, 2003; ACCEPTED APRIL 8, 2004
ADVANCE ACCESS PUBLICATION AUGUST 19, 2004

Two series of anhydrous experiments have been performed in an end-loaded piston cylinder apparatus on a primitive, mantle-derived tholeiitic basalt at 1·0 GPa pressure and temperatures in the range 1060–1330°C. The experimental data provide constraints on phase equilibria, and solid and liquid compositions along the liquid line of descent of primary basaltic magmas differentiating in storage reservoirs located at the base of the continental crust. The first series are equilibrium crystallization experiments on a single basaltic bulk composition; the second series are fractionation experiments where near-perfect fractional crystallization was approached in a stepwise manner using 30°C temperature steps and starting compositions corresponding to the liquid composition of the previous, higher-temperature glass composition. Liquids in the fractional crystallization experiments evolve with progressive SiO_2 increase from basalts to dacites, whereas the liquids in the equilibrium crystallization experiments remain basaltic and display only a moderate SiO_2 increase accompanied by more pronounced Al_2O_3 enrichment. The principal phase equilibria controls responsible for these contrasting trends are suppression of the peritectic olivine + liquid = opx reaction and earlier plagioclase saturation in the fractionation experiments compared with the equilibrium experiments. Both crystallization processes lead to the formation of large volumes of ultramafic cumulates related to the suppression of plagioclase crystallization relative to pyroxenes at high pressures. This is in contrast to low-pressure fractionation of tholeiitic liquids, where early plagioclase saturation leads to the production of troctolites followed by (olivine-) gabbros at an early stage of differentiation.

KEY WORDS: *liquid line of descent; tholeiitic magmas; equilibrium crystallization; fractional crystallization*

INTRODUCTION

Tholeiitic basalts are the most common basaltic magmas erupted at the Earth's surface. They are the predominant magma type at mid-ocean ridges (mid-ocean ridge basalt; MORB), in plume-related oceanic and continental flood basalt provinces, as well as in a number of ocean islands (e.g. Hawaii). Additionally, they also occur in active continental rift zones during advanced stages of continental break-up.

The formation of anhydrous tholeiitic basalts as products of partial melting of upper-mantle peridotite has been well constrained by many experimental studies (including, e.g. Falloon & Green, 1987; Kinzler & Grove, 1992*a*, 1992*b*; Hirose & Kushiro, 1993; Baker & Stolper, 1994; Falloon *et al.*, 2001). Understanding the phase equilibria of basaltic magmas at the Earth's surface and in shallow-level magma chambers has been the target of a large number of experimental studies (e.g. Bowen, 1914, 1928; Andersen, 1915; Yoder & Tilley, 1962; Green & Ringwood, 1967; O'Hara, 1968; Thompson, 1975*b*; Bender *et al.*, 1978; Grove & Bryan, 1983; Nielsen & Dungan, 1983; Baker & Eggler, 1987; Grove & Juster, 1989; Longhi, 1991; Grove *et al.*, 1992; Yang *et al.*, 1996). These experimental data combined with thermodynamic

*Corresponding author. Telephone: 0041 1 632 78 02. E-mail: sam@erdw.ethz.ch
†Present address: Institute of Geological Sciences, Uinversity of Bern, Baltzerstrasse 1–3 3012, Bern, Switzerland

model calculations (e.g. Ghiorso & Sack, 1995; Ghiorso *et al.*, 2002) have provided a basis for the interpretation and understanding of the formation and differentiation of MORB and layered intrusions.

Petrological and geochemical studies of continental flood basalts such as those of Parana–Etendeka, Deccan, Karoo, Siberia and Columbia River Plateau indicate that differentiation of the primary, mantle-derived magmas is a polybaric process, starting at the crust–mantle boundary (e.g. Cox, 1980; Lightfoot *et al.*, 1990). Geophysical studies of rifted continental margins suggest underplating of large volumes of mafic magma at the base of the thinned continental crust during rifting (Mutter *et al.*, 1984; Holbrook & Kelemen, 1993). In the European Alpine realm, exposed deep crustal sections such as the Malenco (Müntener *et al.*, 2000) or the Ivrea–Verbano Zone (Rivalenti *et al.*, 1975, 1984) reveal massive amounts of high-pressure ultramafic to mafic cumulates of tholeiitic affinity. These cumulate rocks have been explained by igneous underplating of the continental crust by basaltic magmas at the crust–mantle boundary under amphibolite- to granulite-facies conditions (Bergantz, 1989). In summary, field, petrological and geochemical studies on tholeiitic igneous rocks unambiguously underline the importance of differentiation processes operating at pressures corresponding to lower-crustal conditions. Petrologic and geochemical (including isotope) data reveal that a number of processes are involved in the differentiation of these tholeiitic magmas: (1) fractional and/or equilibrium crystallization; (2) assimilation of continental lower crust; (3) trapping of interstitial liquids in cumulates; (4) mingling and/or mixing of more evolved with less differentiated magmas in lower-crustal magma chambers; (5) replenishment of magma chambers with less differentiated magmas.

There are only a limited number of experimental studies on the phase relations of anhydrous tholeiite basalt compositions under conditions prevailing in the lower continental crust (e.g. Green & Ringwood, 1967; Thompson 1974, 1975*a*; Baker & Eggler, 1983; Elthon & Scarfe, 1984; Gust & Perfit, 1987; Bartels *et al.*, 1991; Draper & Johnston, 1992; Kinzler & Grove, 1992*a*; Yang *et al.*, 1996). The majority of these experiments were designed to establish near-liquidus phase relations (multiple-saturation experiments), so as to constrain the partial melting conditions and source mineralogy of the basaltic starting material. Consequently, these data generally do not cover the entire temperature range of magmatic differentiation. In addition, the various studies are not always mutually consistent, in particular with respect to olivine and plagioclase stability relations. A number of studies were performed with starting compositions that are not consistent with a primary mantle origin, using bulk compositions with Mg-number [molar $Mg/(Mg + Fe_{tot})$] considerably below 0·70, values inconsistent with equilibration with mantle peridotite (Roedder & Emslie, 1970; Ulmer, 1989).

In addition to the limited set of experiments that are available to constrain the evolution of anhydrous tholeiitic magmas at lower-crustal conditions, there is a fundamental problem in applying equilibrium crystallization experiments to interpret high-pressure crystallization products (ultramafic to mafic lower-crustal cumulate rocks) and their respective differentiated liquids. Cumulate rocks (with all the features typical for solid–liquid separation processes, such as modal and grain-size layering, cumulate textures varying from ad- to orthocumulates) imply fractional crystallization as the predominant differentiation process. Equilibrium crystallization–partial melting experiments on a constant bulk composition cannot simulate this process. In a multi-component natural system it is not straightforward to deduce the liquid line of descent for fractionally crystallized liquids from equilibrium crystallization experiments, in particular if complex peritectic reaction relationships are involved in the crystallization process. Similarly when currently available thermodynamic models (e.g. MELTS and pMELTS, Ghiorso & Sack, 1995; Asimow & Ghiorso, 1998; Ghiorso *et al.*, 2002) are used to calculate the liquid lines of descent of fractionally crystallizing tholeiitic magmas, they result in very different phase relations and liquid compositions from our experimental results and at present such calculations cannot be used to infer the fractionation path of tholeiitic liquids at lower-crustal conditions.

In an attempt to resolve some of the above issues two series of experiments were performed to simulate the liquid line of descent of anhydrous mantle-derived tholeiitic magmas at 1·0 GPa, evolving by fractional and equilibrium crystallization, respectively. We present quantitative data on the phase relations, phase proportions and the compositions of melts and coexisting crystalline products. The differences between the two end-member crystallization processes and the evaluation of their role in the formation of lower continental crustal cumulates is then discussed.

EXPERIMENTAL TECHNIQUES

Experimental strategy

Two contrasting experimental series, subsequently referred to as equilibrium and fractional crystallization experiments, respectively, were performed. The equilibrium crystallization experiments used a constant starting composition (a primitive tholeiitic basalt) and temperature increments of 30°C between successive runs. An approximation to pure fractional crystallization was achieved by a stepwise approach. The liquid compositions were determined in each experiment. The succeeding experiment

Table 1: Starting compositions used for the anhydrous experiments

Sample	SiO_2	TiO_2	Al_2O_3	Cr_2O_3	FeO_{tot}	MnO	MgO	CaO	Na_2O	K_2O	Mg-no.
HK#19	49·10	0·60	15·17	0·36	7·54	0·14	13·10	12·27	1·58	0·08	0·76
HK#19.1	49·07	0·60	15·28	0·36	7·50	0·14	13·04	12·31	1·57	0·08	0·76
HK#19.2	48·67	0·57	14·55	0·34	7·56	0·14	14·81	11·73	1·50	0·08	0·78
fr1	49·78	0·59	14·32	0·36	7·43*	0·15	14·02	11·69	1·58	0·08	0·77
fr2	50·47	0·60	14·78	0·25	7·25*	0·16	12·38	12·30	1·73	0·09	0·75
fr3	51·56	0·72	17·03	0·04	7·80	0·15	8·88	11·33	2·34	0·15	0·67
fr4.1	52·43	0·89	17·54	0·01	8·53	0·13	6·99	10·42	2·86	0·20	0·59
fr5	53·07	0·93	17·85	0·02	8·94*	0·15	5·99	9·49	3·31	0·26	0·54
fr6	56·77	1·37	16·28	0·01	9·89	0·15	3·81	7·26	3·92	0·55	0·41
fr7	62·64	1·97	14·27	0·02	8·99	0·13	1·68	5·20	4·22	0·87	0·25
fr8	64·80	2·06	13·50	0·01	8·35	0·14	1·22	4·52	4·28	1·12	0·21

The starting material HK#19 used in equilibrium crystallization experiments represents a basaltic liquid in equilibrium with a lherzolitic residuum at 1·5 GPa and 1350°C (Hirose & Kushiro, 1993). HK#19.1 is HK#19 + 0·5 wt % pure anorthite seeds. For the fractional crystallization experiment SV44 HK#19.2 [HK#19 + 0·5 wt % anorthite seeds + 5·0 wt % natural forsterite (Fo_{90})] was used. Starting materials fr1—fr8 correspond to the glass compositions of the previous 30°C higher temperature experiment (see Tables 2 and 3).
*FeO_{tot} was corrected for experiments with $\Delta Fe > 2{\cdot}0$ wt % (see Table 2). FeO_{tot} and Mg-number: all Fe as Fe^{2+}.

was then performed at a 30°C lower temperature starting with a synthetic mix of the liquid composition from the previous (higher-temperature) experiment. With this approach we not only simulate fractional crystallization (by removal of all solid phases), but we also obtain a series of experiments that result in variable but relatively high melt fractions (0·98–0·48) that in turn allow us to perform experiments over a large range of differentiation with the possibility to obtain precise liquid compositions. The choice of 30°C temperature increments was guided by the reproducibility, which is approximately ±15°C, and the goal to achieve enough compositional difference between two subsequent experiments that it can be determined quantitatively. Smooth variations of phase relations and liquid compositions are taken as an indication that we did not seriously overstep an important peritectic reaction.

Starting materials

The starting compositions used for the anhydrous experiments at 1·0 GPa are listed in Table 1. Composition HK#19 represents a primitive basaltic glass composition (Mg-number 0·76) derived from dry partial melting experiments performed by Hirose & Kushiro (1993) on KLB1. This composition is in equilibrium with a lherzolitic residue (ol, opx, cpx) at 1·5 GPa and 1350°C.

In a first series of equilibrium crystallization experiments the HK#19 composition was investigated over the temperature range 1300°C to 1060°C. We did not observe any plagioclase crystallization. To test potential plagioclase nucleation inhibition, we added 0·5 wt % pure anorthite seeds to the starting material (HK#19.1) and repeated the experiments. With the added seeds, plagioclase crystallized at temperatures lower than 1150°C, but with the undesirable result that now olivine failed to crystallize in the subliquidus runs and cpx plus opx were the liquidus phases. Therefore, we used the results from experiments conducted with unseeded starting composition HK#19 to interpret near-liquidus phase relations at temperatures between 1300 and 1210°C (Table 1). Lower-temperature phase equilibria, however, were based on the results of experiments performed with the seeded starting material HK#19.1. Experiments conducted at 1150 and 1210°C, i.e. at temperatures lower than the disappearance of olivine in the unseeded experiments, but higher than the occurrence of plagioclase in the seeded experiments, result in identical phase relations (cpx, opx, sp, liq) and similar modal proportions for both starting compositions, HK#19 and HK#19.1. Evidently, small changes in the starting composition have considerable effects on the observed phase equilibria. We attribute these effects to the composition of our starting material, which was purposely chosen to be nearly multiply saturated with a lherzolitic residue (olivine, cpx and opx) at near-liquidus conditions. To ensure that the system is saturated with olivine at the liquidus we added 5 wt % of natural olivine (Fo_{90}) to the starting material HK#19.1. This new composition (HK#19.2) was used as starting point for the fractional crystallization

experiments. Starting materials fr1–fr8 correspond to the glass compositions of the previous experiment at higher temperatures (Tables 1–3) that were synthesized from chemicals for each subsequent fractional crystallization experiment.

The starting materials consist of mixtures of fired synthetic and natural oxides, silicates and carbonates. A mixture of finely ground refractory components (SiO_2, TiO_2, Al_2O_3, $CaAl_2Si_2O_8$, $CaCO_3$, MgO, Cr_2O_3) was fired for 2 h at 1100°C to completely dehydrate the oxides and decarbonize the $CaCO_3$. This mixture was added to the finely ground reactive components (Fe_2SiO_4, MnO, Na_2SiO_3, $KAlSi_3O_8$,) in weight proportions appropriate to obtain 2·5 g of starting material. The final powders were homogenized by re-grinding in an agate mortar for $\frac{1}{2}$ h under ethanol and dried for at least 1 day at 220°C.

Experimental set-up

To minimize Fe loss to the noble metal capsule and to constrain the f_{O_2} near the C–CO_2–CO equilibrium, the Pt–graphite double-capsule technique was applied (Ulmer & Luth, 1991). A graphite container was filled with the powdered starting material and closed with a tight-fitting lid (2·6 mm outer diameter; 1·5 mm inner diameter). The graphite container was placed in a 3·0 mm Pt-capsule and welded shut.

All nominally anhydrous experiments were performed in a solid media high-pressure apparatus at the ETH Zürich. An end-loaded piston cylinder apparatus with a 14 mm bore was used. NaCl–Pyrex–MgO assemblies with a friction correction of −3% applied to the nominal pressure were used to the highest temperatures. Pressure was calibrated against the quartz–coesite transition at 1000°C and 3·07 GPa (Bose & Ganguly, 1995) and the univariant reaction fayalite + quartz = orthoferrosilite at 1000°C and 1·41 GPa (Bohlen *et al.*, 1980). Temperatures were measured with Pt–$Pt_{90}Rh_{10}$ (S-type) and $Pt_{94}Rh_6$–$Pt_{70}Rh_{30}$ (B-type) thermocouples with an estimated accuracy of ±10°C, without taking into account the effect of pressure on the e.m.f. To assess potential 'thermocouple poisoning' of the Pt–Rh thermocouples we continuously monitored the output-power of the thyristor unit; power demand was nearly constant over the duration of the experiment after an initial power increase attributed to thermal equilibration and mechanical relaxation of the assembly.

Analytical methods

All experimental run products were analysed using a five-spectrometer electron microprobe (Cameca SX50) at the Institute for Mineralogy and Petrology, ETH Zürich. A 15 kV accelerating potential, 7 nA beam current and 10 μm beam size were used for analysing the quenched glasses. The crystalline phases were analysed with 20 nA beam current and 1 μm beam size. All elements were analysed for 20 s, except for Na in quenched glasses, for which the counting time was 10 s because of potential Na loss. Depending on the quality of the polished surface of the experimental charges all glass analyses summed between 96 and 100 wt % (Table 3) and have been normalized to 100 wt % for graphic representation, comparison and the calculation of modal proportions.

Modal proportions of phases (glass, olivine ± cpx) of the high-pressure run products reported in Table 2 were estimated using non-weighted least-squares regression analyses balancing the nominal composition of the bulk starting material against the averages of all analysed phases in the experimental charges. Errors indicated in Table 2 are the statistical error calculated by the least-squares regression routine implemented in the EXCEL spreadsheet program. We checked the influence of the renormalization to 100% of the melt phase on the results of the regression calculations by performing a second set of regression calculations using the original, non-renormalized microprobe analyses. Results were identical within statistical error (Table 2). Therefore, to provide internal consistency, i.e. avoiding differences related exclusively to the quality of the surface of the microprobe mounts and hence the total sum of the oxides of the melt analysis, we prefer the results from the calculations performed with the renormalized analyses. For all experiments reported here the sum of the residuals squared (Σr^2) is less than 0·2, except for SV44 (0·79). If the calculated Fe loss (see Table 2 and discussion below) exceeded 2% relative, the least-squares regression was repeated after omitting Fe from the calculation; this resulted in considerably smaller residuals without significant change of modal proportions.

RESULTS

Experimental run conditions, phase assemblages and their calculated proportions, Fe/Mg, Al and Ca/Na K_d values, as well as relative iron losses (ΔFe %), are reported in Table 2. The compositions of crystalline phases and quenched glasses are listed in Table 3.

Iron loss

In all but a few runs a certain amount of Fe was lost to the platinum capsule. Fe loss occurs because of small cracks in the inner graphite capsule. In two runs (SV53, SV54) small amounts of Fe gain were observed, most probably because of small weighing errors. In all runs relative Fe

Table 2: Experimental run conditions, phase assemblage and proportions

Run no.	Starting Material	T (°C)	Time (h)	Run products	Phase proportions (wt %)	K_d(Fe/Mg)		K_d(Al)		K_d(Ca/Na)		ΣR^2	ΔFe (%)
						ol	cpx	opx	cpx	opx	plg		
Equilibrium crystallization													
SV12	HK#19	1300	6·0	liq	100·0(4)								1·60
SV11	HK#19	1270	6·3	liq, ol, sp	97·5(4):2·1(3):0·4(3)	0·34						0·10	6·29
SV13	HK#19	1240	6·0	liq, ol, cpx, sp	94·1(19):4·2(7):1·2(21):0·5(3)	0·33	0·34		0·31			0·19	1·63
SV15	HK#19	1210	6·2	liq, cpx, opx, sp	72·6(5):20·6(6):6·3(3):0·5(1)		0·33	0·32	0·32	0·37		0·01	4·37
SV27	HK#19.1	1180	88·2	liq, cpx, opx, sp	58·5(8):33·3(10):5·6(6):2·6(2)		0·32	0·34	0·38	0·39		0·06	9·99
SV28	HK#19.1	1150	89·0	liq, cpx, opx, sp	52·7(1):35·3(2):9·5(1):2·6(1)		0·31	0·34	0·39	0·36		0·00	9·33
SV25	HK#19.1	1120	114·4	liq, cpx, opx, plg, sp	42·8(41):40·7(10):11·4(18):1·3(33)3·8(5)		0·28	0·31	0·41	0·42	1·71	0·01	6·65
SV24	HK#19.1	1090	95·4	liq, cpx, opx, plg, sp	31·1(56):42·5(17):15·5(26):7·7(50):3·2(9)		0·27	0·29	0·40	0·40	1·76	0·03	8·09
Fractional crystallization													
SV46	HK#19.2	1330	6·7	liq	100(7)								9·43
SV44	HK#19.2	1300	12·0	liq, ol	98·1(12):1·9(10)	0·33						0·79	8·27
SV49	fr1	1270	13·3	liq, ol, cpx, opx, sp	90·1(10):5·9(6):2·0(11):1·2(9):0·8(2)	0·34	0·38	0·34	0·36	0·30		0·03	2·82
SV53	fr2	1240	15·2	liq, cpx, opx	75·1(38):21·9(58):3·0(38)		0·33	0·31	0·35	0·33		0·03	−1·53
SV54	fr3	1210	16·7	liq, cpx, opx plg, sp	68·3(10):18·6(6):2·5(5):9·0(6):1·6(1)		0·38	0·32	0·36	0·28	0·90	0·01	−0·09
SV57	fr4.1	1180	24·0	liq, cpx, plg, sp	80·5(11):12·5(6):6·2(7):0·8(1)		0·39		0·35		0·96	0·03	5·52
SV58	fr5	1150	26·0	liq, cpx, plg sp	48·1(6):24·1(3):24·3(4):3·5(1)		0·34		0·25		1·00	0·01	0·11
SV61	fr6	1120	84·8	liq, cpx, plg, sp	49·6(8):21·2(6):24·1(4):5·1(1)		0·28		0·17		0·79	0·02	0·00
SV63	fr7	1090	169·5	liq, cpx, plg, sp, qtz, ilm	78·0(39):6·3(4):12·2(23):1·3(2):1·7(10):0·5(2)		0·30		0·16		0·83	0·01	1·63
SV64	fr8	1060	185·2	liq, cpx, plg, qtz, ilm	52·2(46):10·3(10):26·8(25):5·3(13):2·4(3)		0·26		0·14		0·94	0·12	1·17

Starting materials fr1—fr8 correspond to the glass compositions of the previous 30°C higher temperature experiment (see Table 3). Fe/Mg K_d values are calculated as $(FeO_{sol} \times MgO_{liq})/(FeO_{liq} \times MgO_{sol})$. Al K_d values are calculated as $Al_2O_{3\ sol}/Al_2O_{3\ liq}$. Ca/Na K_d values are calculated as $(CaO_{plg} \times Na_2O_{liq})/(CaO_{liq} \times Na_2O_{plg})$. ΔFe is the difference between the FeO content of the bulk starting composition and the FeO in the bulk composition calculated by mass balance. Negative values indicate relative iron gain in relative weight percent. Phase proportions are calculated by least-squares regressions. ΣR^2 indicates the quality of the regression. Units in parentheses represent the 2σ error from regression analysis. Accordingly, 94·1(19) is read as 94·1 ± 1·9.

Table 3: Electron microprobe analyses of run products in wt %

Run no.	π	*n*	SiO_2	TiO_2	Al_2O_3	Cr_2O_3	FeO_{tot}	MnO	MgO	CaO	Na_2O	K_2O	Total	Mg-no.	X_{An}
Equilibrium crystallization															
HK#19	gl		47·53(22)	0·65(2)	14·45(2)	0·34(4)	6·42(16)	0·15(3)	12·49(10)	12·19(14)	1·87(6)	0·07(1)	96·18	0·76	
SV11	gl	11	48·98(23)	0·55(3)	14·67(3)	0·25(4)	6·87(15)	0·15(4)	12·29(11)	12·36(10)	1·65(5)	0·08(1)	97·86	0·77	
	ol	10	41·17(13)	0·01(1)	0·07(1)	0·16(2)	9·16(7)	0·12(2)	49·95(37)	0·32(1)	<0·01	<0·01	100·97	0·90	
	sp	5	0·09(13)	0·20(2)	36·81(180)	32·68(150)	9·92(19)	<0·1	18·69(16)	0·28(3)	0·02(1)	<0·01	98·63	0·78	
SV13	gl	9	48·17(37)	0·67(3)	15·91(3)	0·19(5)	7·13(15)	0·16(5)	11·33(8)	12·67(14)	1·66(7)	0·08(1)	97·98	0·75	
	ol	10	39·72(38)	0·02(1)	0·15(8)	0·16(3)	9·86(15)	0·16(2)	49·77(23)	0·35(2)	0·02(1)	<0·01	100·20	0·89	
	cpx	13	52·57(91)	0·26(7)	4·98(68)	1·26(20)	4·05(27)	0·15(12)	19·62(43)	18·09(61)	0·32(3)	<0·01	101·30	0·90	
	sp	6	0·52(32)	0·19(3)	41·82(75)	26·89(76)	9·92(40)	<0·01	19·05(10)	0·42(10)	0·02(2)	<0·01	98·83	0·77	
SV15	gl	8	47·15(43)	0·65(18)	17·76(18)	0·09(4)	7·59(19)	0·22(2)	9·79(11)	11·48(26)	2·05(7)	0·09(7)	96·88	0·70	
	cpx	8	52·04(93)	0·41(22)	5·96(108)	0·54(15)	4·95(47)	0·17(4)	18·95(63)	17·47(60)	0·42(7)	<0·01	100·91	0·87	
	opx	15	52·77(104)	0·17(6)	6·74(98)	0·62(9)	7·41(73)	0·21(2)	29·79(50)	2·49(13)	0·09(2)	0·01(1)	100·30	0·88	
	sp	6	0·30(9)	0·17(1)	55·75(22)	12·54(37)	10·21(9)	0·07(1)	19·92(7)	0·2(1)	0·02(1)	<0·01	99·17	0·77	
SV27	gl	10	49·81(26)	0·72(3)	18·53(3)	0·08(4)	7·30(11)	0·13(4)	8·54(20)	10·73(8)	2·18(8)	0·12(1)	98·14	0·68	
	cpx	12	51·34(47)	0·3(4)	7·1(52)	1(15)	4·89(36)	0·14(1)	17·89(47)	17·87(56)	0·44(2)	<0·01	100·95	0·87	
	opx	7	53·17(58)	0·16(4)	7·38(85)	0·65(17)	8·44(49)	0·17(3)	28·89(73)	2·11(15)	0·08(1)	<0·01	101·05	0·86	
SV28	gl	9	49·77(19)	0·78(5)	19·36(5)	0·03(3)	7·13(13)	0·17(3)	7·38(20)	10·31(14)	2·55(8)	0·15(2)	97·63	0·65	
	cpx	12	50·47(72)	0·41(6)	7·69(81)	0·46(8)	5·14(64)	0·16(1)	16·95(48)	19·04(45)	0·47(2)	<0·01	100·80	0·85	
	opx	9	52·70(23)	0·19(2)	7·18(42)	0·53(11)	9·60(82)	0·19(1)	28·82(45)	1·86(12)	0·07(1)	<0·01	101·13	0·84	
	sp	7	0·33(31)	0·11(2)	62·51(118)	5·09(119)	11·45(56)	<0·01	20·48(52)	0·15(3)	0·02(2)	<0·01	100·16	0·77	
SV25	gl	10	50·19(35)	0·76(5)	18·88(5)	0·02(1)	7·17(13)	0·20(4)	5·96(21)	9·35(20)	2·89(16)	0·17(2)	95·57	0·60	
	cpx	8	50·55(48)	0·49(4)	8·13(60)	0·49(5)	5·44(51)	0·18(3)	16·31(61)	19·29(43)	0·52(4)	<0·01	101·40	0·84	
	opx	9	52·26(21)	0·26(3)	8·23(48)	0·41(10)	10·26(24)	0·20(2)	26·97(24)	2·24(11)	0·10(2)	<0·01	100·93	0·82	
	plg	10	49·66(22)	0·03(1)	31·73(22)	0·01(1)	0·31(5)	0·02(1)	0·2(6)	15·84(22)	2·86(9)	0·02(1)	100·68		0·75
	sp	6	0·42(25)	0·13(1)	62·29(77)	4·95(72)	12·25(50)	0·02(2)	20·22(9)	0·16(4)	0·03(2)	<0·01	100·47	0·75	
SV24	gl	10	51·74(31)	0·81(3)	19·45(3)	0·02(2)	7·02(15)	0·14(3)	5·10(35)	8·72(19)	3·13(25)	0·19(2)	96·33	0·56	
	cpx	13	49·76(32)	0·62(7)	8·05(38)	0·51(8)	5·95(39)	0·19(3)	15·74(41)	19·20(48)	0·51(2)	<0·01	100·53	0·83	
	opx	13	51·58(39)	0·26(5)	8·01(52)	0·36(10)	10·97(52)	0·20(3)	27·39(63)	1·77(12)	0·08(2)	<0·01	100·63	0·82	
	plg	10	49·40(43)	0·02(1)	32·06(38)	0·02(1)	0·32(5)	0·01(1)	0·14(6)	15·28(24)	3·11(18)	<0·01	100·38		0·73
	sp	6	0·38(21)	0·15(1)	61·67(75)	5·87(87)	13·57(25)	0·05(4)	18·21(60)	0·18(4)	0·02(2)	<0·01	100·10	0·70	

Run no.	π	*n*	SiO_2	TiO_2	Al_2O_3	Cr_2O_3	FeO_{tot}	MnO	MgO	CaO	Na_2O	K_2O	Total	Mg-no.	X_{An}
Fractional crystallization															
HK#19.2	gl		48·00(34)	0·56(2)	13·89(2)	0·34(2)	6·66(12)	0·17(2)	13·50(12)	11·48(10)	1·61(7)	0·08(1)	96·28	0·78	
SV44 = fr1	gl	13	48·44(23)	0·57(1)	13·94(1)	0·35(2)	6·61(13)	0·15(2)	13·64(10)	11·38(6)	1·54(4)	0·08(1)	96·68	0·79	
	ol	11	41·06(15)	0·01(1)	0·06(1)	0·24(1)	8·01(14)	0·13(1)	50·91(26)	0·30(1)	0·02(1)	<0·01	100·75	0·91	
SV49 = fr2	gl	11	48·73(24)	0·57(1)	14·26(1)	0·24(2)	6·57(10)	0·15(2)	11·95(12)	11·87(10)	1·76(7)	0·10(1)	96·22	0·76	
	ol	6	40·61(24)	<0·10	0·07(1)	0·17(1)	9·34(14)	0·15(1)	49·69(35)	0·28(2)	0·01(1)	<0·01	100·32	0·90	
	cpx	21	52·38(42)	0·21(4)	5·39(40)	1·23(12)	4·18(30)	0·12(2)	20·15(53)	16·94(61)	0·35(2)	<0·01	100·94	0·90	
	opx	12	54·68(40)	0·09(1)	4·52(30)	1·28(9)	5·88(27)	0·13(2)	31·57(23)	2·45(13)	0·06(1)	<0·01	100·66	0·91	
	sp	5	0·19(19)	0·21(1)	33·19(102)	37·24(70)	10·49(30)	0·23(2)	18·41(14)	0·26(14)	0·01(1)	<0·01	100·21	0·77	
SV53 = fr3	gl	10	50·64(21)	0·71(3)	16·73(3)	0·04(2)	7·66(11)	0·15(3)	8·72(6)	11·13(9)	2·30(6)	0·14(2)	98·20	0·67	
	cpx	15	52·70(34)	0·23(4)	5·99(75)	0·60(6)	5·64(23)	0·15(1)	19·19(94)	15·19(59)	0·45(5)	0·02(1)	100·17	0·86	
	opx	20	54·06(27)	0·12(1)	5·57(31)	0·55(3)	7·88(14)	0·15(1)	29·02(29)	2·75(17)	0·09(1)	<0·01	100·18	0·87	
SV54 = fr4·1	gl	10	51·64(22)	0·88(3)	17·27(3)	0·01(1)	8·40(13)	0·13(3)	6·88(8)	10·26(10)	2·82(7)	0·20(1)	98·50	0·59	
	cpx	18	52·04(57)	0·46(10)	6·26(79)	0·17(2)	7·56(50)	0·17(3)	16·33(93)	17·15(87)	0·57(5)	0·01(1)	100·73	0·79	
	opx	12	54·10(36)	0·20(3)	4·83(58)	0·14(2)	10·93(11)	0·19(2)	27·77(26)	2·56(11)	0·11(2)	<0·01	100·82	0·82	
	plg	12	52·71(36)	0·04(2)	29·34(48)	0·01(1)	0·51(16)	0·02(1)	0·31(15)	13·37(28)	4·08(11)	0·06(1)	100·44		0·64
	sp	6	0·21(4)	0·09(1)	66·04(57)	0·02(2)	13·11(39)	0·11(2)	19·45(15)	0·15(1)	0·02(1)	<0·01	99·18	0·73	
SV57 = fr5	gl	14	52·24(23)	0·91(4)	17·57(4)	0·02(1)	8·20(15)	0·14(3)	5·90(10)	9·34(5)	3·26(13)	0·26(1)	97·83	0·54	
	cpx	17	50·54(63)	0·70(8)	6·16(96)	0·04(1)	9·35(57)	0·19(1)	16·18(46)	16·01(42)	0·60(3)	<0·01	99·78	0·76	
	plg	13	53·06(52)	0·04(1)	28·27(50)	0·01(1)	0·60(22)	0·01(1)	0·24(7)	12·29(33)	4·49(16)	0·07(1)	99·09		0·60
	sp*	3	2·55(137)	0·19(2)	64·65(99)	0·11(6)	12·67(33)	0·09(1)	19·04(43)	0·76(26)	0·09(4)	<0·01	97·60	0·71	
SV58 = fr6	gl	11	55·87(56)	1·34(8)	16·02(8)	0·01(1)	9·73(24)	0·14(2)	3·74(14)	7·14(16)	3·85(36)	0·54(3)	98·41	0·41	
	cpx	39	51·53(41)	0·66(6)	4·03(54)	0·03(1)	12·89(45)	0·29(1)	14·61(48)	15·78(63)	0·65(3)	<0·01	100·49	0·67	
	plg	35	57·79(67)	0·08(1)	27·56(43)	<0·01	0·59(10)	0·01(1)	0·14(3)	9·93(42)	5·35(28)	0·15(1)	101·60		0·51
	sp	5	0·39(31)	0·43(19)	63·21(62)	0·01(1)	23·33(68)	0·17(2)	13·28(98)	0·18(9)	0·03(2)	<0·01	101·02	0·50	
SV61 = fr 7	gl	7	60·66(46)	1·91(4)	13·81(4)	0·02(2)	8·70(23)	0·13(2)	1·63(8)	5·03(9)	4·09(32)	0·85(4)	96·83	0·25	
	cpx	26	50·92(20)	0·97(12)	2·44(16)	0·06(1)	17·88(53)	0·38(2)	12·12(39)	15·25(76)	0·59(5)	<0·01	100·62	0·55	
	plg	30	63·26(70)	0·10(2)	24·19(44)	<0·01	0·58(5)	0·01(1)	0·07(1)	6·21(43)	6·42(33)	0·27(2)	101·12		0·35
	sp	9	0·15(7)	0·69(9)	60·64(29)	0·02(1)	29·45(24)	0·18(1)	9·20(12)	0·11(2)	0·01(1)	<0·01	100·44	0·36	

Table 3: continued

Run no.	π	*n*	SiO_2	TiO_2	Al_2O_3	Cr_2O_3	FeO_{tot}	MnO	MgO	CaO	Na_2O	K_2O	Total	Mg-no.	X_{An}
SV63 = fr8	gl	8	63·06(31)	2·01(4)	13·14(4)	0·01(1)	8·13(17)	0·14(2)	1·19(4)	4·40(4)	4·16(5)	1·09(2)	97·33	0·21	
	cpx	12	50·09(21)	1·30(5)	2·24(21)	0·04(1)	19·73(70)	0·42(2)	9·63(20)	15·56(88)	0·52(3)	0·02(1)	99·53	0·47	
	plg	19	62·83(104)	0·09(1)	24·15(54)	<0·01	0·47(4)	0·01(1)	0·03(1)	6·12(56)	6·96(14)	0·31(3)	100·97		0·32
	qtz	3	98·92(8)	0·02(1)	0·01(1)	<0·01	0·16(15)	0·01(1)	0·02(1)	0·03(1)	0·01(1)	<0·01	99·19		
	sp	8	0·13(7)	0·76(12)	59·42(39)	<0·01	31·81(26)	0·26(2)	5·82(16)	0·09(2)	0·02(1)	<0·01	98·32	0·24	
	ilm	6	0·18(10)	52·72(43)	0·29(1)	0·05(1)	41·47(21)	0·48(1)	2·08(9)	0·20(4)	0·01(1)	<0·01	97·48	0·08	
SV64	gl	10	65·72(21)	1·32(4)	12·27(4)	0·02(1)	7·53(21)	0·14(1)	0·58(2)	3·32(3)	4·13(6)	2·15(3)	97·17	0·12	
	cpx	10	48·66(21)	0·85(5)	1·82(9)	0·03(1)	26·32(25)	0·63(4)	7·89(20)	12·75(130)	0·39(4)	0·03(1)	99·35	0·35	
	plg	20	63·44(71)	0·11(3)	23·36(28)	<0·01	0·62(5)	0·02(1)	0·02(1)	5·60(32)	7·39(15)	0·65(4)	101·21		0·29
	qtz	3	99·49(26)	0·02(1)	0·03(1)	<0·01	<0·01	<0·01	0·02(1)	0·04	0·01	0·01	99·63		
	ilm	7	0·15(3)	51·79(30)	0·25(2)	0·07(1)	44·70(33)	0·54(1)	1·39(12)	0·18(2)	0·02(1)	0·04(1)	99·30	0·05	

FeO_{tot} and Mg-number: all Fe as Fe^{2+}. Units in parentheses indicate standard errors (2σ) from average analysis. Accordingly, 1·69(5) should be read as 1·69 ± 0·05. Glass compositions referring to starting materials fr1—fr8 are given in column for run number. π, phase; *n*, number of analyses.

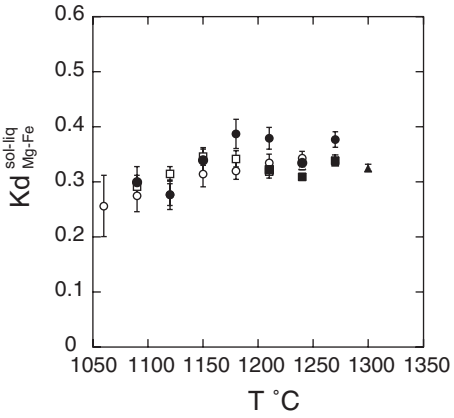

Fig. 1. Fe–Mg partitioning [$K_{d(Fe-Mg)}^{sol-liq}$ = $(Fe/Mg)_{solid}/(Fe/Mg)_{liquid}$] between crystals and melt as a function of temperature (°C) for equilibrium (open symbols) and fractional crystallization (filled symbols) experiments. Triangles, olivines; circles, cpx; squares, opx. Error bars indicate 2σ standard errors.

losses or gains were lower than 10% (estimates basing on mass balance calculations), therefore a relatively constant bulk composition was maintained during the experiments.

Attainment of equilibrium

Close approximation to equilibrium is indicated by Fe–Mg partitioning between the solid phases and the quenched liquids (expressed as K_d values). The Fe/Mg olivine–liquid K_d values vary between 0·34 and 0·33. They are identical to the K_d values obtained for basaltic compositions at 1·0 GPa (Ulmer, 1989) and for mantle partial melting experiments (Gaetani & Grove, 1998) with an f_{O_2} constrained by the C–CO_2–CO equilibrium in this temperature range. The pyroxene–liquid Fe–Mg K_d values in our experiments are in the same range as those of mantle partial melting experiments performed by Gaetani & Grove (1998). For a single experiment, the Fe–Mg K_d values for orthopyroxene (opx) and clinopyroxene (cpx) are identical within error. For the equilibrium crystallization experiments they decrease from 0·34 to 0·27 with falling temperature (Fig. 1), whereas for the fractional crystallization experiments the trend is not so obvious, and the variability for the cpx–melt Fe–Mg K_d values is higher (0·39–0·26). However, overall we observe a decrease of the K_d values with increasing differentiation consistent with increasing polymerization of coexisting liquids, as observed, for example, by Kushiro & Mysen (2002) for olivine–liquid Fe–Mg partitioning. In most experimental charges pyroxenes and plagioclase exhibit chemical zonation. In particular, the opx of run SV53 (1240°C, fractionation experiment) shows sector zoning with Al-poor (3·2 ± 0·2 wt % Al_2O_3) and Al-rich sectors (5·8 ± 0·3 wt % Al_2O_3). Analyses of rim compositions of cpx were not possible in a number of runs because of their small grain size (5–20 μm). Plagioclase shows normal zonation with decreasing anorthite content from cores to rims (e.g. SV57 plagioclase profile from core to rim: X_{An} 0·63–0·55). Anorthite-rich cores observed in some experiments result from the pure anorthite seeds, indicating that chemical equilibrium was not fully achieved. An additional indication for a successful approach to equilibrium is provided by the quality of mass balance calculations performed with average analyses of solid and quenched liquid phases.

Estimate of oxygen fugacity

The oxygen fugacity of the piston cylinder experiments performed at 1·0 GPa and 1330°C to 1060°C was calculated with the empirical equation of Ulmer & Luth (1991) and Frost & Wood (1995), resulting in $\log f_{O_2}$ of −8·2 to −10·8 with falling temperature. These values apply only if the hydrogen fugacity in our system is minimal and therefore the graphite stability reaches its maximum in the C–COH system. To minimize the f_{H_2} in our experiments we used MgO spacers around, below and above the capsule. Such assemblies provide very oxidizing conditions, several log units above the Ni–NiO equilibrium, and hence impose a rather low intrinsic hydrogen fugacity, as verified by Kägi (2000) for identical assemblies at 1·0 GPa pressure. In addition, this approach minimizes the production of H_2O by hydrogen diffusion from the surrounding assembly material and provides a close approach to anhydrous (water-free) experiments. Small amounts of CO_2 produced from oxidation of graphite cannot be completely excluded. The calculated oxygen fugacities of the quenched liquids in equilibrium with graphite are 2–1·5 log units below the Ni–NiO equilibrium. Fe^{3+}/Fe^{2+} ratios calculated with the equation of Kress & Carmichael (1991) vary between 0·05 and 0·03. Consequently, the molar Mg-number is calculated assuming all Fe as Fe^{2+}. These values vary between 0·76 and 0·56 in glasses obtained in the equilibrium crystallization experiments and from 0·78 to 0·12 in glasses produced in the fractional crystallization experiments.

The f_{O_2} of both equilibrium and fractional crystallization experiments is buffered along the C–CO–CO_2 equilibrium and, therefore, our experimental system represents an open system with respect to oxygen. Natural systems are often regarded as closed systems where the Fe^{3+}/Fe^{2+} ratio of the crystallizing assemblage exerts the dominant control on oxygen fugacity (e.g. Muan, 1958). However, our experiments were purposely run at low f_{O_2} to keep the Fe^{3+}/Fe^{2+} very low. Consequently, the open-system behaviour with respect to oxygen that is intrinsic to our experimental setup should not dramatically affect the liquid line of descent as inferred for more oxidizing systems [at f_{O_2} corresponding to

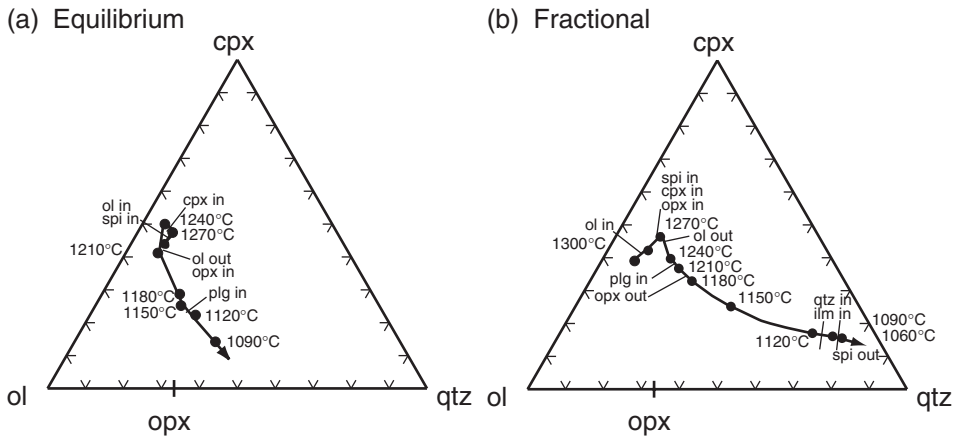

Fig. 2. Normative pseudoternary cpx–olivine–quartz projection of the liquid lines of descent (glass compositions) for anhydrous (a) equilibrium and (b) fractional crystallization experiments at 1·0 GPa. Normalization into six components in oxygen units (olivine, cpx, plg, qtz, orthoclase, oxide) and the projection scheme are after Grove *et al.* (1992); compositions are projected from plagioclase, orthoclase and oxide. Temperatures and phase appearance (in) or disappearance (out) are noted along the liquid lines of descent for each projection point of the melt compositions.

fayalite–magnetite–quartz (FMQ)] by Ghiorso & Carmichael (1985).

Crystallization sequence and melt fractions

The calculated melt fractions decrease from 97·5% to 31·1% in the equilibrium crystallization experiments between 1270 and 1090°C. Olivine and Cr-rich spinel are the liquidus phases at 1270°C followed by cpx at 1240°C. At 1210°C olivine disappears from the crystallizing assemblage. Orthopyroxene crystallizes concomitantly with cpx and spinel from 1210°C to 1150°C. Plagioclase joins cpx, opx and spinel at 1120°C and 1090°C.

In the fractional crystallization series olivine is the liquidus phase at 1300°C (as a result of the addition of 5 wt % Fo_{90} olivine; see above). In contrast to the equilibrium crystallization experiments the solid phases at 1270°C are olivine, cpx, opx and spinel, followed by cpx and opx at 1240°C. In this series the first occurrence of plagioclase is located at 1210°C coprecipitating with cpx, opx and spinel. Between 1180°C and 1120°C cpx, plagioclase and spinel crystallize. At 1090°C quartz and ilmenite are stable with cpx, plagioclase and spinel, and at 1060°C spinel disappears from the solid phase assemblage consisting of cpx, plagioclase, quartz and ilmenite. Melt fractions vary between 48 and 98 wt % in the single fractionation steps. It is, however, more useful to use cumulative melt fractions, i.e. the melt masses calculated for each fractionation step are multiplied; hence, the cumulative melt fractions represent the amount of liquid left relative to the initial starting composition (HK#19.2). The cumulative melt fractions range from 98·1% to 3·7%. The melt fractions obtained by mass balance calculations are in good agreement with the melt fractions calculated independently assuming K_2O behaves as a completely incompatible oxide component (neglecting that a small fraction of K_2O enters plagioclase as the orthoclase component).

DISCUSSION

Liquid lines of descent at 1·0 GPa

The anhydrous liquid lines of descent at 1·0 GPa are shown in the ol–cpx–qtz projection in Fig. 2. The quenched glass compositions have been recalculated into mineral end-member components and are projected onto the ol–cpx–qtz plane of the basalt tetrahedron projected from spinel and plagioclase following the method of Grove *et al.* (1992). The liquid lines of descent of equilibrium and fractional crystallization show contrasting trends in this projection. In both series the liquids evolve from olivine-normative to quartz-normative compositions with falling temperature. However, the phase equilibria and extent of silica enrichment are very different for the two series. The major differences are the temperature of plagioclase saturation (1120°C in the equilibrium as opposed to 1210°C in the fractional crystallization experiments) and the stability of opx, which continuously crystallizes below 1210°C in the equilibrium experiments but occurs only between 1270 and 1210°C in the fractionation series. The contrasting opx stability in the two series is clearly linked to the suppression of the peritectic reaction olivine + liquid = opx in the fractional crystallization experiments. The delayed plagioclase crystallization and the persistence of opx for

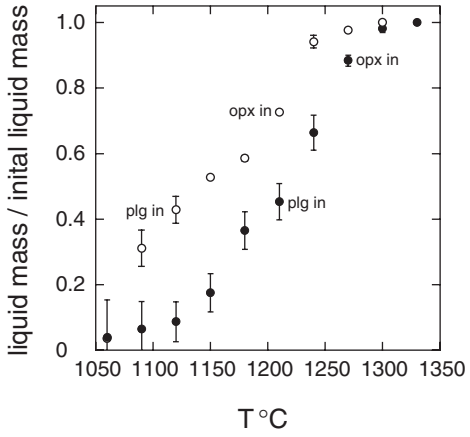

Fig. 3. Liquid mass/initial liquid mass vs temperature for equilibrium (○) and fractional crystallization (●) experiments. For fractionation experiments the cumulative melt fractions (product of melt fraction in each fractionation step) are plotted. Error bars indicate 2σ standard errors calculated from the least-squares regression analysis (Table 2).

equilibrium crystallization drive the liquids towards an alumina-rich basaltic andesite composition at falling temperatures. In contrast, the liquids in the fractional crystallization experiments range from basaltic to dacitic compositions with increasing differentiation, as a result of both the absence of opx at low temperatures, resulting in continuous silica enrichment, and early plagioclase saturation suppressing the Al_2O_3 enrichment in the derivative liquids.

Melt fractions

Figure 3 illustrates the liquid mass relative to the initial liquid mass (the primary basaltic composition HK#19 and HK#19.2, respectively) as a function of temperature. Melt fractions for both crystallization processes decrease steeply after the first appearance of pyroxenes. This is in contrast to the liquid mass vs initial liquid mass ratios in the fractional crystallization of MORB liquids calculated at lower pressures (200 MPa), where the large increase of the crystallization rate is predicted to occur at the onset of plagioclase saturation that follows after olivine precipitation (Kelemen & Aharonov, 1998). At high pressure (1·0 GPa), pyroxene crystallization precedes plagioclase crystallization as a result of the shift of the cotectic lines between plagioclase and pyroxene (and olivine) towards the plagioclase apex in the cpx–olivine–plagioclase ternary system (Morse, 1994). At a given temperature the remaining melt fraction is considerably lower after fractional crystallization compared with equilibrium crystallization (e.g. at 1090°C: 6·8% fractional crystallization, 31% equilibrium crystallization). Fractional crystallization results in much higher crystallization rates when compared with initial liquid mass because low variance cotectics (e.g. qtz-saturated cotectics) are reached by fractional crystallization that are not attainable by equilibrium crystallization as a result of bulk system constraints and peritectic reaction relationships between phenocrysts and residual liquid.

Liquid compositions

The compositional effects of the two contrasting crystallization processes are highlighted in Fig. 4, where oxide components of glasses are plotted versus Mg-number. Silica enrichment is very different for the two series; at 1090°C equilibrium crystallization results in a liquid with 53·7 wt % SiO_2 whereas fractional crystallization produces dacitic liquids with 64·8 wt % SiO_2. Likewise the Mg-number are 0·56 and 0·21, respectively, emphasizing the effects of fractional crystallization (Fig. 4a). At similar Mg-number considerable differences are observed for Al_2O_3 and FeO_{tot}. With increasing differentiation, the iron content of the bulk solid fraction (sum of crystallized phases, total solid composition) exceeds the iron content of the coexisting liquid. FeO_{tot} reaches a maximum in the liquid of 9·8 wt % in fractional and 7·8 wt % in equilibrium crystallization experiments (Fig. 4c). The strong decrease in FeO_{tot} concentration in the liquids of the fractionation series at temperatures below 1150°C is due to spinel (hercynitic) and ilmenite precipitation. Alumina content increases in the liquid phase until plagioclase starts to crystallize; maximum Al_2O_3 content reaches about 17·8 wt % Al_2O_3 in the fractional crystallization experiments, whereas suppressed plagioclase crystallization in the equilibrium experiments leads to an accumulation of up to 20·2 wt % Al_2O_3 (Fig. 4b). Al_2O_3 enrichment paired with a moderate SiO_2 increase in the equilibrium crystallization experiments produces a liquid line of descent directed towards the opx–qtz join and close to peraluminous compositions (Fig. 2). By contrast, constant SiO_2 enrichment with only moderate initial alumina increase followed by alumina decrease drives the melts obtained by fractional crystallization towards the qtz–cpx join. Titanium behaves as an incompatible element in both series until ilmenite saturation occurs in the fractional crystallization experiments (Fig. 4d).

The early crystallization of a spinel phase and the suppression of the olivine + liquid = opx peritectic reaction are responsible for the constant increase of silica in the fractionation experiments. This is in contrast to the tholeiitic trends observed at lower pressures, as originally defined by Fenner (1929) and exemplified by the tholeiitic lavas of the Thingmuli volcano (Carmichael, 1964) or layered intrusions such as the Skaergaard (Wager, 1960; Hunter & Sparks, 1987). Grove & Baker (1984) reported a crystallization sequence at 1 atm that starts with olivine

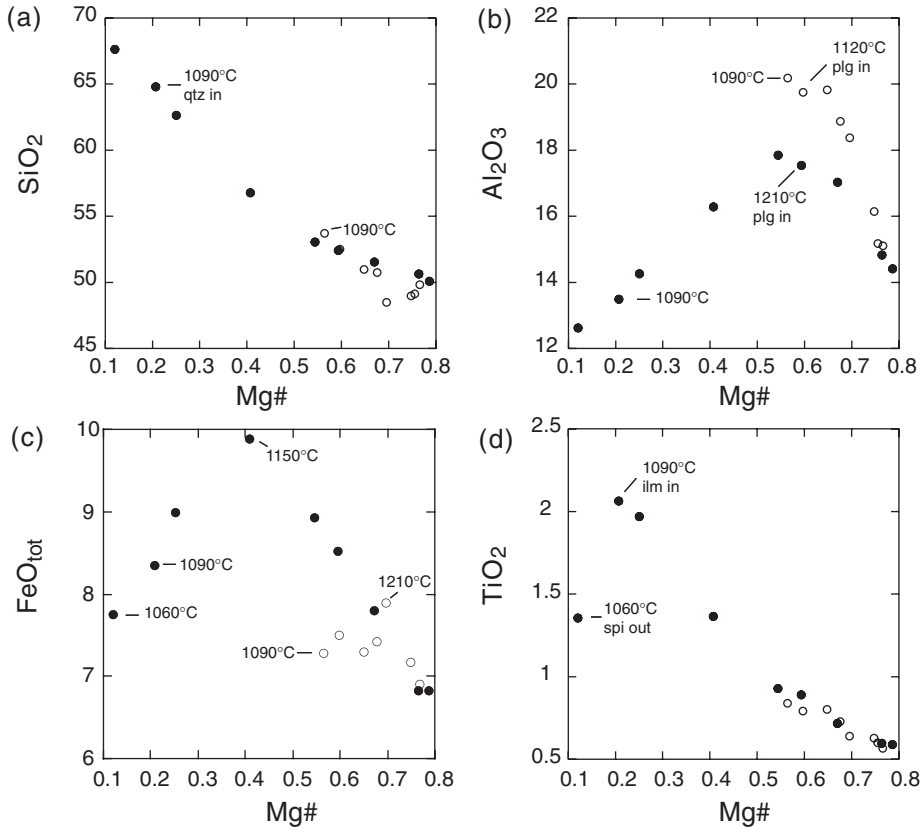

Fig. 4. Variation of selected oxide components (in wt %) as a function of Mg-number [= molar MgO/(MgO + FeO)] for equilibrium (○) and fractional crystallization (●) experiments. Mg-numbers are calculated assuming all Fe as Fe^{2+}. (a) SiO_2; (b) Al_2O_3; (c) FeO_{tot}; (d) TiO_2.

or olivine plus plagioclase as the liquidus phases, followed by olivine, plagioclase and augite. At lower temperature, olivine and liquid are in reaction relationship and plagioclase, augite and pigeonite are the crystallizing phases. The model calculations of Grove & Baker based on low-pressure phase equilibria indicate that silica enrichment at low pressures is the consequence of late disappearance of olivine and magnetite crystallization in Fe-enriched derivative liquids.

Comparison with thermodynamic models (MELTS and pMELTS)

Figure 5 presents a comparison of the liquid lines of descent for a fractionally crystallized primary tholeiitic basalt from this study with the liquid lines of descent calculated for the same composition with the thermodynamic algorithms MELTS and pMELTS (Ghiorso & Sack, 1995; Asimow & Ghiorso, 1998; Ghiorso *et al.*, 2002). MELTS has been developed to calculate solid–liquid phase equilibria at low to moderate pressures over a wide range of natural igneous compositions, whereas pMELTS has been optimized for partial melting calculations exclusively for peridotitic bulk compositions including high-pressure (>1·0 GPa) conditions. Two different approaches were chosen: (1) MELTS or pMELTS was allowed to perform forward fractional crystallization calculations with no constraints, except f_{O_2} buffered by the C–CO–CO_2 equilibrium and a fixed pressure of 1·0 GPa (Fig. 5a); (2) calculations were forced along the liquid line of descent constrained by the experiments, i.e. we performed a series of equilibrium crystallization calculations using the liquid compositions obtained in each 30°C step in the experiments (Fig. 5b). We evaluated the difference between experimental and calculated melt fractions, compared the residual phases from the experiments with those calculated by MELTS or pMELTS, and illustrate a 'best-fit' calculated liquid line of descent (Fig. 5b). The main purpose of this exercise was to evaluate the applicability of both the MELTS and the pMELTS code to calculate liquid lines of descent at high pressures and to identify potential shortcomings of the currently implemented codes. Inspection of Fig. 5a clearly reveals that straightforward fractionation calculations at high pressures do not result in liquid lines of descent consistent with the experiments, but produce markedly contrasting trends of decreasing modal quartz, ultimately leading to nepheline-normative (silica-undersaturated) liquid compositions. MELTS calculates opx

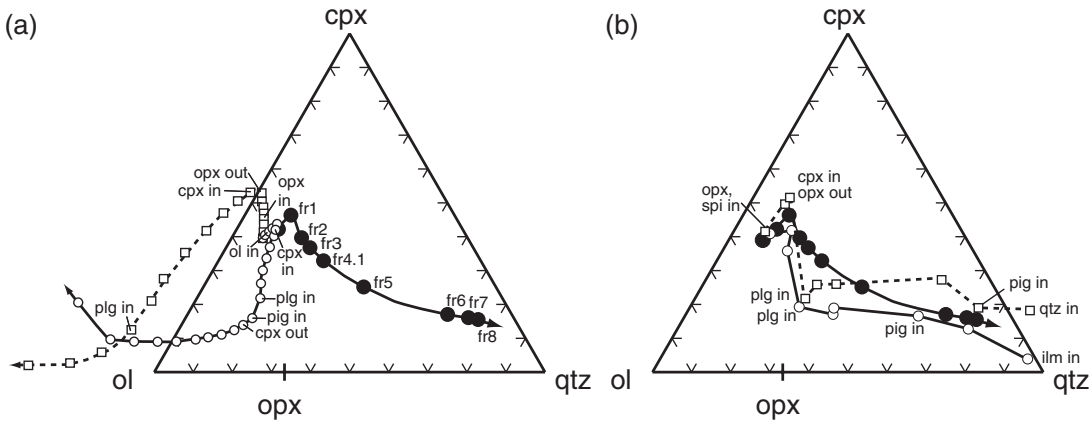

Fig. 5. Pseudoternary cpx–olivine–quartz projection (for details see caption of Fig. 2) of glass compositions from anhydrous fractional crystallization experiments at 1·0 GPa (●) and two fractionation trends calculated with MELTS (□) and pMELTS (○) (Ghiorso & Sack, 1995; Asimow & Ghiorso, 1998; Ghiorso *et al.*, 2002). (a) Liquid compositions calculated for fractional crystallization of composition HK#19.2 (Table 1) at 1·0 GPa. (b) Liquid compositions obtained from a series of equilibrium crystallization experiments at 1·0 GPa using as starting compositions the liquid compositions of the fractional crystallization experiments (HK#19.2, fr1–fr8, Tables 1–3) to force calculations along the experimentally constrained liquid line of descent.

as a liquidus phase, followed by cpx only and late plagioclase crystallization. The lack of olivine and the dominance of opx in the early fractionation steps drive the liquids rapidly into the nepheline-normative phase-field; the turning point corresponds to the cessation of opx and the onset of cpx crystallization, and results in a vector pointing away from the cpx corner. In contrast, pMELTS calculations result dominantly in cpx as the near-liquidus phase accompanied by minor olivine precipitation and liquids enter the nepheline-normative phase-field after extensive crystallization of cpx and later plagioclase. This is predominantly due to an overestimation of modal cpx and an underestimation of the role of spinel and other Fe–Ti-oxide phases (ilmenite) during pMELTS calculation of fractional crystallization. In addition, at the turning point in the crystallization path shown in Fig. 5a, which corresponds to the cessation of spinel and the onset of plagioclase crystallization, the calculated cpx composition suddenly changes from a 'normal' augitic cpx to a cpx with a pigeonite-like (low-CaO) chemistry. This compositional change, combined with a rather siliceous calculated plagioclase composition, is mainly responsible for the inflection towards the olivine corner and ultimately drives the calculated liquid compositions into the SiO_2-undersaturated field. In the case of 'forced' calculations (Fig. 5b) the liquid lines of descent are constrained closely to the experimentally derived one. In the case of pMELTS the difference, again, is clearly related to overestimation of the modal amount of cpx crystallizing from the parent liquids leading to a systematic deviation of the calculated liquid line of descent away from the cpx apex. Calculations performed with MELTS initially show the same behaviour as pMELTS calculations, leading to compositions shifted towards the olivine–quartz baseline. Subsequent crystallization overestimates the plagioclase fractions compared with the experimentally derived liquid line of descent, and consequently the trend is reversed and the compositions shift towards the cpx apex (Fig. 5b). In summary, whereas thermodynamically based calculations of igneous phase equilibria at high pressures in differentiated bulk compositions are clearly still premature, our experimental results can be used to investigate several aspects of current codes such as MELTS or pMELTS. Specifically, experimental equilibrium data such as those presented here can certainly be used to constrain the thermodynamic mixing properties of solid and liquid phases at high pressure in differentiated basaltic compositions to generate phase diagrams that are needed to interpret and understand the evolution of common basaltic magmas in deep-seated magma systems through polybaric, fractional crystallization.

Mineral compositions and mineral–liquid exchange reactions

Pyroxene

Figure 6 depicts the experimental pyroxene compositions in the pyroxene quadrilateral. Coexisting cpx–opx pairs are connected with continuous tie-lines. With falling temperature the enstatite component in cpx decreases, whereas the ferrosilite component increases (Mg-number equilibrium crystallization: cpx: 0·90–0·83, opx: 0·88–0·82; Mg-number fractional crystallization: cpx: 0·90–0·35, opx: 0·91–0·82). Dashed lines indicate the 1·0 GPa isotherms for coexisting pyroxenes in the CaO–MgO–FeO–SiO_2 system of Lindsley (1983). The compositions of coexisting cpx–opx pairs plot on isopleths that exceed the experimental temperatures considerably. Lindsley's

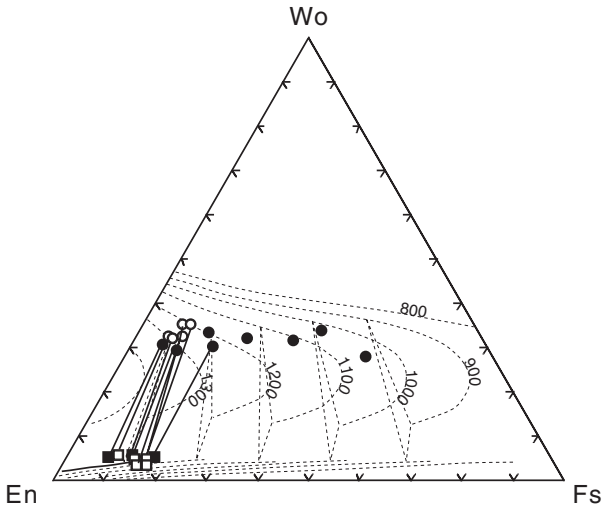

Fig. 6. Experimental pyroxene compositions in a molar wollastonite–enstatite–ferrosilite ternary diagram. Symbols: circles, cpx; squares, opx; open symbols, equilibrium crystallization experiments; filled symbols, fractional crystallization experiments. Coexisting cpx–opx pairs are connected with continuous tie-lines. Projection scheme and isotherms according to Lindsley (1983).

(1983) calibration is based on alumina-free to alumina-poor clinopyroxene and overestimates the temperatures for alumina-rich (augitic) clinopyroxenes up to 200°C. This effect can mainly be attributed to the normalization scheme used for the calculation of the quadrilateral components. Tetrahedral Al is exclusively assigned to Ca-Tschermak's components and subtracted from the wollastonite component, resulting in a low wollastonite component compared with Al-free pyroxenes with identical Ca content. For the equilibrium crystallization experiments the Al_2O_3 content of cpx increases from 4·98 to 8·13 wt %, whereas the Al_2O_3 contents of cpx in the fractional crystallization experiments have a narrower compositional range from 5·39 to 6·26 wt % until plagioclase joins the crystallizing assemblage; thereafter the Al_2O_3 content of cpx decreases to 1·82 wt %.

Pyroxene–liquid relationships

A closer inspection of the behaviour of alumina in pyroxenes reveals that the partitioning of Al between pyroxene and coexisting liquid, as expressed by the log K_d values [=molar Al_2O_3 (pyx)/Al_2O_3 (liq)] and plotted as a function of the inverse temperature (Fig. 7a), shows two contrasting trends for the equilibrium and fractional crystallization experiments. The K_d values for cpx and opx in the equilibrium crystallization experiments are identical within error. They exhibit a small but significant increase with falling temperature, similar to the K_d values observed for water-undersaturated experiments on basaltic andesites and high Mg-andesites performed by

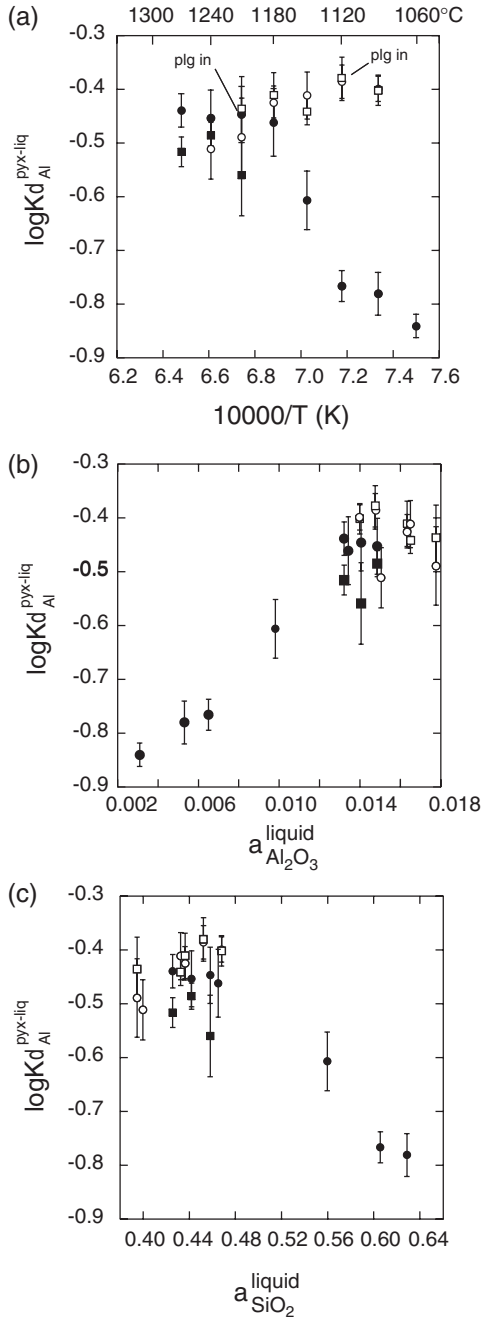

Fig. 7. (a) Logarithm of the Al_2O_3 partition coefficients between pyroxene and melt as a function of reciprocal temperature (K) for equilibrium (open symbols) and fractional crystallization (filled symbols) experiments. Circles, cpx; squares, opx. Error bars indicate 2σ standard errors. (b) Logarithm of the Al_2O_3 partition coefficients between pyroxene and melt as a function of calculated Al_2O_3 activities for liquid compositions from equilibrium (open symbols) and fractional crystallization (filled symbols) experiments. (c) Logarithm of the Al_2O_3 partition coefficients between pyroxene and melt as a function of calculated SiO_2 activities for liquid compositions from equilibrium (open symbols) and fractional crystallization (filled symbols) experiments. The activities were calculated for each experimental glass composition using the MELTS supplemental calculator (Ghiorso & Sack, 1995; Asimow & Ghiorso, 1998) at 1·0 GPa and its experimental temperature (1330–1060°C).

Müntener *et al.* (2001). In the fractional crystallization experiments opx exhibits slightly lower K_d values than cpx. The K_d values are similar to those of the equilibrium experiments until plagioclase joins the crystallizing assemblage, when the values decrease dramatically with falling temperature. This contrasting behaviour cannot be explained by crystal chemical variations alone. Neither Al(VI) nor Al(IV), nor any combination of these, shows a systematic variation with K_d. We also tested the variation of the K_d values as a function of liquid polymerization as expressed by NBO/T (Mysen *et al.*, 1982) and did not find a correlation. However, there is a fundamental difference between the compositions of liquids that coexist with pyroxenes at a given temperature, for SiO_2 and Al_2O_3, between the equilibrium and fractional crystallization experiments. To test a potential dependence of the Al-partitioning on the liquid composition we calculated the Al_2O_3 and SiO_2 activities of the liquids using the supplemental calculator provided on the MELTS web-page of Mark Ghiorso (http://CTserver.uchicago.edu) at the pressure–temperature conditions of the runs; the results for the Al_2O_3 and SiO_2 activities are plotted in Fig. 7b and c as a function of log K_d. Clear positive and negative correlations between the Al pyroxene–liquid K_d and the calculated activities of Al_2O_3 and SiO_2 in the liquid phase of the fractional crystallization experiments are observed. Equilibrium crystallization experiments show only limited variation of silica and alumina activities, consistent with the limited variation in pyroxene–liquid Al K_d. We interpret these correlations as a clear indication that the partitioning of Al between coexisting liquid and pyroxene is strongly controlled by the thermodynamic properties of the liquid phase. The complementary behaviour of the variation of log K_d with the calculated alumina and silica activities of the liquid phase indicates that the Tschermak's components in pyroxenes (Ca or $MgAl_2SiO_6$ component in cpx and opx, respectively) are strong functions of the activities of the Tschermak's components in the liquid phase. The contrasting compositions of the liquid phases responsible for the variation in the activities of alumina and silica, respectively, are related to the crystallization sequence. Increasing alumina contents and activities are a consequence of fractionation of olivine and pyroxene and suppressed plagioclase crystallization in the equilibrium experiments; decreasing alumina contents in the fractionation experiments are the result of the early crystallization of the Al-rich phase plagioclase.

Plagioclase

The anorthite content of plagioclases in the fractional crystallization experiments ranges from X_{An} 0·64 to 0·29. Anorthite content correlates positively with the Mg-number of coexisting clinopyroxene until quartz and ilmenite join the crystallizing assemblage, when the slope flattens out (Fig. 8). The two plagioclase compositions obtained from the equilibrium crystallization experiments have X_{An} of 0·75 and 0·73, respectively, and plot close to the end of the array defined by the fractionation experiments (Fig. 8).

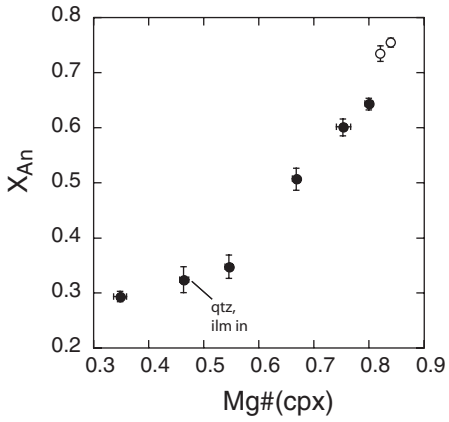

Fig. 8. Anorthite content (X_{An}) of plagioclase vs Mg-number [= molar $Mg/(Mg + Fe^{2+})$] of coexisting cpx from equilibrium (○) and fractional crystallization (●) experiments. Error bars indicate 2σ standard errors. Mg-number is calculated assuming all Fe as Fe^{2+}.

The variation of the CaO/Na_2O ratio expressed in wt % between plagioclase and liquid is shown in Fig. 9. In a series of hydrous high-pressure experiments, Sisson & Grove (1992) demonstrated that these are positively correlated at constant H_2O contents. The variation of anorthite content as function of H_2O content in the liquid phase for constant bulk composition was determined by Yoder (1969). Sisson & Grove (1992) reported increasing K_d values $[=(CaO/Na_2O)_{plag}/(CaO/Na_2O)_{liq}]$ with increasing H_2O contents in the melt phase and also with increasing pressure in anhydrous experiments. In our experiments, the plagioclases of the fractional crystallization experiments define a linear function with an average K_d of 0·90 ± 0·08. The average K_d of the equilibrium crystallization experiments is about 1·73. Both datasets are within the range of K_d values reported for anhydrous experiments at 0·9–1·1 GPa in the literature, which vary between 0·80 and 1·85 (Bartels *et al.*, 1991; Draper & Johnston, 1992; Fram & Longhi, 1992; Kinzler & Grove, 1992*a*). A closer look reveals a rather subtle difference between liquids that crystallize quite contrasting plagioclase compositions in the two series: at near-constant CaO/Na_2O ratio in the liquid, e.g. comparing experiment SV57 (fractional, 1180°C) with SV25 (equilibrium, 1120°C), the composition of the liquid phase is nearly identical but the CaO/Na_2O of coexisting plagioclase is 2·74 and 5·54, respectively. Calculation of activities of selected components in the liquid phase (see results above obtained using the MELTS supplemental calculator) reveals nearly identical activities (at pressure

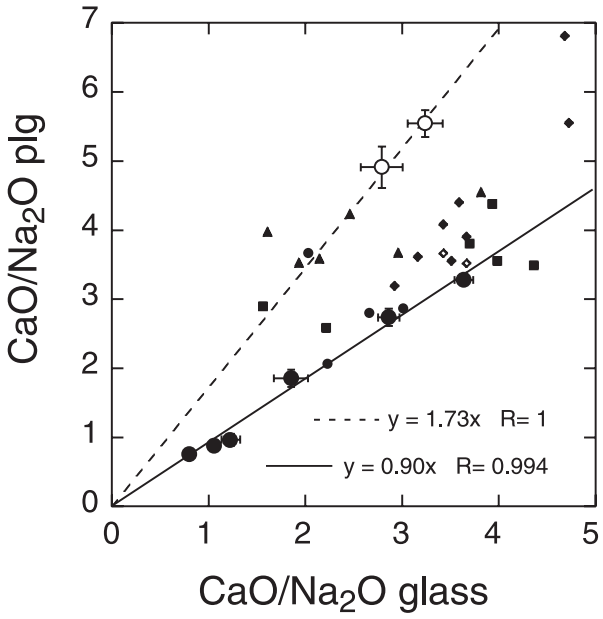

Fig. 9. CaO/Na_2O ratios (wt %) of plagioclase vs coexisting quenched liquids (glasses) of equilibrium (○) and fractional crystallization (●) experiments. Small symbols represent data from anhydrous experiments at 0·9–1·1 GPa pressure: diamonds, Bartels *et al.* (1991); triangles, Draper & Johnston (1992); circles, Fram & Longhi (1992); squares, Kinzler & Grove (1992*a*).

and temperature conditions corresponding to the experiments) except for the Na_2SiO_3 and $KAlSiO_4$ activities, which are the alkali components chosen to represent the chemical system. Both Na_2SiO_3 and $KAlSiO_4$ activities are approximately double those in the liquid obtained from our fractional crystallization experiments (SV57). Hence, we interpret the systematic variation of the CaO/Na_2O partitioning between plagioclase and liquid again as being controlled by the thermodynamic properties of the liquid phase, specifically the alkali species, in particular the Na_2SiO_3 activities of the coexisting liquid. However, we cannot *a priori* exclude some temperature effect as the two experiments discussed above have 60°C different temperatures.

Spinel

Experimentally produced spinels cover the compositional range from Mg–Cr–Al-rich (picotitic) to hercynitic compositions. Their Mg-number ranges from 0·78 to 0·70 in the equilibrium crystallization experiments and from 0·77 to 0·24 in the fractional crystallization experiments. Fe^{3+} contents of the spinels, calculated assuming stoichiometry and charge balance, are always lower than 0·03 per formula unit, consistent with the low rather f_{O_2} conditions imposed by the graphite sample containers. The Cr/Al ratios decrease with progressive crystallization from 0·60 to 0·05 in equilibrium and from 0·75 to 0·0 in just two fractionation steps in the fractional crystallization experiments.

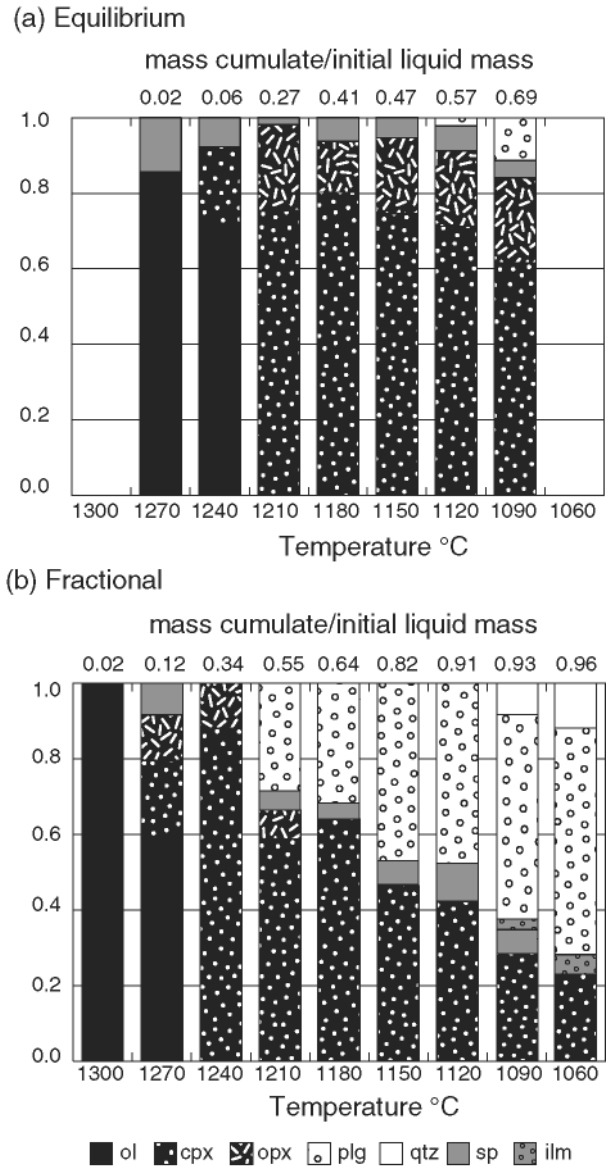

Fig. 10. Schematic representation of weight fractions of calculated modal compositions of cumulates as function of temperature of (a) equilibrium and (b) fractional crystallization experiments. Top labels indicate the (accumulated) amount of solids crystallized. For fractionation experiments the cumulative solid fractions [=1 – (product of liquid fraction in each fractionation step)] are indicated.

'Cumulate' compositions derived from the experiments

This experimental study indicates that anhydrous crystallization of primary tholeiitic basalts at 1·0 GPa should produce large amounts of ultramafic cumulates prior to plagioclase saturation. Table 4 provides the calculated compositions of cumulate assemblages for each crystallization step (in wt %). Figure 10 illustrates the modal

Table 4: Experimental solid compositions in wt % calculated from mineral proportions and electron microprobe analyses of solid run products listed in Tables 2 and 3

Run no.	Residual solids	SiO_2	TiO_2	Al_2O_3	Cr_2O_3	FeO_{tot}	MnO	MgO	CaO	Na_2O	K_2O	Total	Mg-no.
Equilibrium crystallization													
SV11	Spinel dunite	35·22	0·04	5·39	4·87	9·27	0·11	45·42	0·31	0·01	0·00	100·64	0·90
SV13	Spinel wehrlite	39·32	0·08	4·35	2·44	8·68	0·15	41·25	3·97	0·08	0·00	100·32	0·89
SV15	Spinel websterite	51·24	0·35	7·06	0·78	5·61	0·17	21·44	13·73	0·34	0·01	100·73	0·87
SV27	Spinel websterite	48·36	0·27	10·21	1·68	5·71	0·14	19·50	14·63	0·36	0·00	100·85	0·86
SV28	Spinel websterite	48·21	0·35	10·54	0·72	6·37	0·16	19·52	14·58	0·37	0·01	100·83	0·85
SV25	Plg-bearing spinel websterite	47·56	0·41	12·18	0·76	6·77	0·17	18·45	14·50	0·45	0·01	101·26	0·83
SV24	Gabbronorite	47·79	0·45	13·27	0·67	6·81	0·17	16·72	13·95	0·68	0·01	100·52	0·81
Fractional crystallization													
SV44	Dunite	41·06	0·01	0·06	0·24	8·01	0·13	50·91	0·30	0·02	0·00	100·75	0·92
SV49	Spinel lherzolite	41·28	0·07	4·45	3·62	7·98	0·15	38·95	3·88	0·09	0·00	100·47	0·90
SV53	Websterite	52·87	0·22	5·94	0·59	5·91	0·15	20·37	13·70	0·41	0·02	100·17	0·86
SV54	Gabbronorite	49·71	0·30	15·80	0·11	6·10	0·13	12·83	14·06	1·50	0·02	100·57	0·79
SV57	Gabbro	49·15	0·47	15·70	0·03	6·72	0·13	11·25	14·17	1·81	0·03	99·46	0·75
SV58	Gabbro	51·00	0·37	19·06	0·02	7·83	0·15	7·74	11·98	2·81	0·07	101·05	0·64
SV61	Diorite	51·64	0·53	18·75	0·03	10·81	0·19	6·08	9·39	3·31	0·13	100·84	0·50
SV63	Quartz diorite	57·00	1·70	17·54	0·01	8·58	0·15	3·36	7·86	4·00	0·18	100·37	0·41
SV64	Quartz diorite	60·95	3·02	14·42	0·01	8·80	0·19	1·91	6·29	4·51	0·40	100·49	0·28

FeO_{tot} and Mg-number: all Fe as Fe^{2+}.

proportions of liquid and solid phases obtained in the equilibrium and fractional crystallization experiments. Equilibrium and fractional crystallization experiments result in 52 ± 5 wt % and 45 ± 10 wt % of ultramafic cumulates. The crystallization of dunites (ol ± sp) and wehrlites (ol + cpx + sp) for equilibrium and dunites (ol) and lherzolites (ol + cpx + opx + sp) for fractional crystallization experiments is followed by spinel websterites (cpx + opx + sp) and gabbronorites (sp + cpx + opx + plg) as the solid assemblages crystallizing from the magma. Lower-temperature cumulate assemblages in the fractional crystallization experiments are dominated by gabbro (sp + cpx + plg) before the onset of qtz crystallization (qtz-diorites).

The opx/cpx (wt %) ratios of the experimentally derived ultramafic or mafic cumulates vary between 0·36 and 0·17 for the equilibrium crystallization experiments; fractional crystallization experiments result in opx/cpx ratios of 0·60 for the lherzolitic cumulate, 0·14 for the websterite and 0·13 for the gabbronorite. Anhydrous (equilibrium crystallization) experiments on a basaltic composition at 1·0 GPa conducted by Draper & Johnston (1992) were characterized by even lower opx/cpx ratios between 0·18 and 0·03. Water-undersaturated experiments on basaltic andesite and high-Mg andesite bulk composition by Müntener *et al.* (2001) at 1·2 GPa resulted in a decrease of the opx/cpx ratio with falling temperature and increasing water contents in the coexisting melts, from 2·90 to 0·32.

The amount of plagioclase increases in both types of crystallization experiments with increasing differentiation, producing plagioclase-bearing websterites (2 wt % plg) and gabbronorites (11 wt % plg) in the equilibrium crystallization experiments, and gabbronorites (28 wt % plg) followed by gabbros (32–47 wt % plg) and (qtz)-diorites (48–60 wt % plg) in the fractional crystallization experiments.

A comparison of the experimentally derived cumulate compositions with natural lower-crustal ultramafic or mafic cumulates is not straightforward. The calculated cumulate compositions correspond to pure adcumulates rarely observed in layered cumulate rocks. The majority of cumulates are meso- to orthocumulates with a considerable amount of trapped intercumulus liquid. In the investigated system the presence of intercumulus liquid will most probably lead to the following compositional modifications of the calculated cumulate compositions (and modes): (1) progressive crystallization of the intercumulus liquid approaching closed-system (equilibrium) crystallization behaviour will lead to the precipitation of plagioclase in ultramafic cumulate assemblages; (2) opx-poor cumulates produced by fractional crystallization will be subjected to an increase of the opx content as a result of peritectic reactions of the intercumulus liquid with the olivine–cpx–plg assemblages. This argument is in line with observations from lower-crustal cumulate rocks from the Southern Alpine Ivrea–Verbano Zone (Rivalenti *et al.*, 1984): (1) ultramafic or mafic layered rocks show a systematic deviation of the mineral modes towards higher opx/cpx ratios when compared with the experimentally derived cumulates; (2) some gabbroic rocks contain pyroxenes with high Mg-number and rather sodic plagioclases, indicative of late, closed-system intercumulus crystallization of plagioclase.

CONCLUSIONS

The present experimental study, performed at 1·0 GPa, 1060–1330°C, aimed to constrain the phase equilibria and the compositions of liquids and residual solids along the liquid line of descent of anhydrous, mantle-derived primary magmas at the base of the continental crust. The two contrasting series of experiments, simulating equilibrium (closed-system) and fractional (open-system) crystallization, result in different evolution trends. Liquids in the fractional crystallization experiments evolve with progressive silica increase from basalt to dacite, whereas liquids in the equilibrium crystallization experiments remain basaltic and display only a moderate SiO_2 increase accompanied by more pronounced alumina enrichment. The principal phase equilibria controls responsible for these contrasting trends are suppression of the peritectic olivine + liquid = opx reaction, and earlier plagioclase saturation in the fractionation experiments compared with the equilibrium experiments. In contrast to tholeiitic differentiation trends at low pressure (1 bar), suppressed plagioclase crystallization and the persistence of spinel crystallization cause continuous silica enrichment with increasing differentiation at high pressure. As a consequence, crystallization processes operating in the lower continental crust or at the base of the crust (1·0 GPa pressure, ~35 km depth) lead to the production of large volumes of ultramafic cumulates (34–57% of the initial liquid mass) prior to the crystallization of gabbroic assemblages.

The compositional variations of pyroxenes and plagioclase are also influenced by the crystallization process. In fractional crystallization experiments, the Al content systematically decreases at lower temperatures whereas for equilibrium crystallization it does not. Thermodynamic calculations using the MELTS supplemental calculator indicate that the Al activity in the liquid exerts a fundamental control on Al partitioning between liquid and pyroxenes. Likewise, different anorthite contents in plagioclase at similar CaO/Na_2O ratios in the liquid are controlled by Na and K activity in the residual liquid. This conclusion is somewhat contrary to the current trend in crystal–liquid partitioning studies that assigns most of the variation

in crystal–liquid partitioning to the thermodynamic and mechanical properties of the solid phase through the lattice strain model (e.g. Matsui *et al.*, 1977; Blundy & Wood, 1994), and emphasizes the potential importance of liquid composition as an important factor in controlling crystal–liquid partitioning.

ACKNOWLEDGEMENTS

This work was supported by the Swiss National Science Foundation (grant 2000-61894.00/1). We would like to express our thanks to Yaoling Niu, who kindly invited us to contribute to this special volume in honour of Michael O'Hara. We would like to acknowledge the thorough and constructive reviews provided by Bjørn Mysen, Mark Ghiorso and David Draper. Special thanks go to Marjorie Wilson for a perfect editorial job that facilitated the revision of the manuscript considerably.

REFERENCES

Andersen, O. (1915). The system anorthite–forsterite–silica. *American Journal of Science, 4th Series* **39**, 407–454.

Asimow, P. D. & Ghiorso, M. S. (1998). Algorithmic modifications extending MELTS to calculate subsolidus phase relations. *American Mineralogist* **83**, 1127–1131.

Baker, D. R. & Eggler, D. H. (1983). Fractionation paths of Atka (Aleutians) high alumina basalts: constraints from phase relations. *Journal of Volcanology and Geothermal Research* **18**, 387–404.

Baker, D. R. & Eggler, D. H. (1987). Compositions of anhydrous and hydrous melts coexisting with plagioclase, augite, and olivine or low-Ca pyroxene from 1 atm to 8 kbar: application to Aleutian volcanic center of Atka. *American Mineralogist* **72**, 12–28.

Baker, M. B. & Stolper, E. M. (1994). Determining the composition of high-pressure mantle melts using diamond aggregates. *Geochimica et Cosmochimica Acta* **58**, 2811–2827.

Bartels, K. S., Kinzler, R. J. & Grove, T. L. (1991). High pressure phase relations of primitive high-alumina basalts from Medicine Lake volcano, northern California. *Contributions to Mineralogy and Petrology* **108**, 253–270.

Bender, J. F., Hodges, F. N. & Bence, A. E. (1978). Petrogenesis of basalts from the project FAMOUS area: experimental study from 0 to 15 kbar. *Earth and Planetary Science Letters*, 277–302.

Bergantz, G. W. (1989). Underplating and partial melting; implications for melt generation and extraction. *Science* **245**, 1093–1095.

Blundy, J. D. & Wood, B. J. (1994). Prediction of crystal–melt partitioning coefficients from elastic moduli. *Nature* **372**, 452–454.

Bohlen, S. R., Essene, E. J. & Boettcher, A. L. (1980). Reinvestigations and applications of olivine–quartz–orthopyroxene barometry. *Earth and Planetary Science Letters* **47**, 1–10.

Bose, K. & Ganguly, J. (1995). Quartz–coesite revisited: reversed experimental determinations at 500–1000 degrees C and retrieved thermochemical properties. *American Mineralogist* **80**, 231–238.

Bowen, N. L. (1914). The ternary system diopside–forsterite–silica. *American Journal of Science, 4th Series* **33**, 551–573.

Bowen, N. L. (1928). *The Evolution of the Igneous Rocks*. Princeton, NJ: Princeton University Press.

Carmichael, I. S. E. (1964). The petrology of Thingmuli, a Tertiary volcano in eastern Iceland. *Journal of Petrology* **5**, 435–460.

Cox, K. G. (1980). A model for flood basalt volcanism. *Journal of Petrology* **21**, 629–650.

Draper, D. S. & Johnston, A. D. (1992). Anhydrous *PT* phase relations of an Aleutian high-MgO basalt: an investigation of the role of olivine–liquid reactions in the generation of arc high-alumina basalts. *Contributions to Mineralogy and Petrology* **112**, 501–519.

Elthon, D. & Scarfe, C. M. (1984). High-pressure phase equilibria of a high-magnesia basalt and the genesis of primary oceanic basalts. *American Mineralogist* **69**, 1–15.

Falloon, T. J. & Green, D. H. (1987). Anhydrous partial melting of MORB pyrolite and other peridotite compositions at 10 kbar: implications for the origin of primitive MORB glasses. *Mineralogy and Petrology* **37**, 181–219.

Falloon, T. J., Danyushevsky, L. V. & Green, D. H. (2001). Peridotite melting at 1 GPa: reversal experiments on partial melt compositions produced by peridotite–basalt sandwich experiments. *Journal of Petrology* **42**, 2363–2390.

Fenner, C. N. (1929). The crystallization of basalts. *American Journal of Science* **18**, 225–253.

Fram, M. S. & Longhi, J. (1992). Phase equilibria of dikes associated with Proterozoic anorthosite complexes. *American Mineralogist* **77**, 605–616.

Frost, D. J. & Wood, B. J. (1995). Experimental measurements of the graphite C–O equilibrium and CO_2 fugacities at high temperatures and pressure. *Contributions to Mineralogy and Petrology* **121**, 303–308.

Gaetani, G. A. & Grove, T. L. (1998). The influence of water on melting of mantle peridotite. *Contributions to Mineralogy and Petrology* **131**, 323–346.

Ghiorso, M. S. & Carmichael, I. S. E. (1985). Chemical mass transfer in magmatic processes. II. Application in equilibrium crystallization, fractionation and assimilation. *Contributions to Mineralogy and Petrology* **90**, 121–141.

Ghiorso, M. S. & Sack, R. O. (1995). Chemical mass transfer in magmatic processes IV. A revised and internally consistent thermodynamic model for the interpretation and extrapolation of liquid–solid equilibria in magmatic systems at elevated temperatures and pressures. *Contributions to Mineralogy and Petrology* **119**, 197–212.

Ghiorso, M. S., Hirschmann, M. M., Reiners, P. W. & Kress, V. C. I. (2002). The pMELTS: a revision of MELTS aimed at improving calculation of phase relations and major element partitioning involved in partial melting of the mantle at pressures up to 3 GPa. *Geochemistry, Geophysics, Geosystems* **3**, 10.1029/2001GC000217.

Green, D. H. & Ringwood, A. E. (1967). The genesis of basaltic magmas. *Contributions to Mineralogy and Petrology* **15**, 103–190.

Grove, T. L. & Baker, M. B. (1984). Phase equilibrium controls on the tholeiitic versus calc-alkaline differentiation trends. *Journal of Geophysical Research* **89**, 3253–3274.

Grove, T. L. & Bryan, W. B. (1983). Fractionation of pyroxene-phyric MORB at low pressure: an experimental study. *Contributions to Mineralogy and Petrology* **84**, 293–309.

Grove, T. L. & Juster, T. C. (1989). Experimental investigations of low-Ca pyroxene–liquid equilibria at 1-atm in natural basaltic and andesitic liquids. *Contributions to Mineralogy and Petrology* **103**, 287–305.

Grove, T. L., Kinzler, R. J. & Bryan, W. B. (1992). Fractionation of mid-ocean ridge basalt (MORB). In: Phipps Morgan, J., Blackman, D. K. & Sinton, J. M. (eds) *Mantle Flow and Melt Generation at Mid-ocean Ridges. Geophysical Monograph, American Geophysical Union* **71**, 281–310.

Gust, D. A. & Perfit, M. R. (1987). Phase relations of a high-Mg basalt from the Aleutian island arc: implications for primary island arc basalts and high Al basalts. *Contributions to Mineralogy and Petrology* **97**, 7–18.

Hirose, K. & Kushiro, I. (1993). Partial melting of dry peridotites at high pressures: determination of compositions of melts segregated from peridotite using aggregates of diamond. *Earth and Planetary Science Letters* **114**, 477–489.

Holbrook, W. S. & Kelemen, P. (1993). Large igneous province on the US Atlantic margin and implications for magmatism during continental break up. *Nature* **364**, 433–436.

Hunter, R. H. & Sparks, R. S. J. (1987). Differentiation of the Skaergaard intrusion. *Contributions to Mineralogy and Petrology* **95**, 451–461.

Kägi, R. (2000). The liquid line of descent of hydrous, primary, calc-alkaline magmas at elevated pressure. An experimental approach. Ph.D. thesis, ETH Zurich.

Kelemen, P. & Aharonov, E. (1998). Periodic formation of magma fractures and generation of layered gabbros in the lower crust beneath oceanic spreading ridges. In: Buck, W. R., Delaney, P. T., Karson, J. A. & Lagabrielle, Y. (eds) *Faulting and Magmatism at Mid-ocean Ridges. Geophysical Monograph, American Geophysical Union* **106**, 267–289.

Kinzler, R. J. & Grove, T. L. (1992*a*). Primary magmas of mid-ocean ridge basalts 1. Experiments and methods. *Journal of Geophysical Research* **97**, 6885–6906.

Kinzler, R. J. & Grove, T. L. (1992*b*). Primary magmas of mid-ocean ridge basalts 2. Applications. *Journal of Geophysical Research* **97**, 6907–6926.

Kress, V. C. & Carmichael, I. S. E. (1991). The compressibility of silicate liquids containing Fe_2O_3 and the effect of composition, temperature, oxygen fugacity and pressure on their redox state. *Contributions to Mineralogy and Petrology* **108**, 82–92.

Kushiro, I. & Mysen, B. O. (2002). A possible effect of melt structure on the Mg–Fe^{2+} partitioning between olivine and melt. *Geochimica et Cosmochimica Acta* **66**, 2267–2272.

Lightfoot, P. C., Hawkesworth, C. J., Devey, C. W., Rogers, N. W. & Van Calsteren, P. W. C. (1990). Source and differentiation of Deccan Trap lavas; implications of geochemical and mineral chemical variations. *Journal of Petrology* **31**, 1165–1200.

Lindsley, D. H. (1983). Pyroxene thermometry. *American Mineralogist* **68**, 477–493.

Longhi, J. (1991). Comparative liquidus equilibria of hypersthene-normative basalts at low pressures. *American Mineralogist* **76**, 785–800.

Matsui, Y., Onuma, N., Nagasawa, H., Higuchi, H. & Banno, S. (1977). Crystal structure control in trace element partitioning between crystal and magma. *Bulletin de Liaison de la Société Française de Minéralogie et de Cristallographie* **100**, 315–324.

Morse, S. A. (1994). *Basalts and Phase Diagrams. An Introduction to the Quantitative Use of Phase Diagrams in Igneous Petrology*. Malabar, FL: Krieger.

Muan, A. (1958). Phase equilibria at high temperatures in oxide systems involving changes in oxidation states. *American Journal of Science* **256**, 171–207.

Mutter, J. C., Talwani, M. & Stoffa, P. L. (1984). Evidence for a thick oceanic crust adjacent to the Norwegian margin. *Journal of Geophysical Research* **89**, 483–502.

Müntener, O., Hermann, J. & Trommsdorff, V. (2000). Cooling history and exhumation of lower-crustal granulite and upper mantle (Malenco, Eastern Central Alps). *Journal of Petrology* **41**, 175–200.

Müntener, O., Kelemen, P. & Grove, T. L. (2001). The role of H_2O during crystallization of primitive arc magmas at uppermost mantle conditions and genesis of igneous pyroxenites: an experimental study. *Contributions to Mineralogy and Petrology* **141**, 643–658.

Mysen, B. O., Virgo, D. & Seifert, F. A. (1982). The structure of silicate melts: implications for chemical and physical properties of natural magma. *Reviews of Geophysics and Space Physics* **20**, 353–383.

Nielsen, R. L. & Dungan, M. A. (1983). Low pressure mineral–melt equilibria in natural anhydrous mafic systems. *Contributions to Mineralogy and Petrology* **84**, 310–326.

O'Hara, M. J. (1968). The bearing of phase equilibria studies in synthetic and natural systems on the origin and evolution of basic and ultrabasic rocks. *Earth-Science Reviews* **4**, 69–133.

Rivalenti, G., Garuti, G. & Rossi, A. (1975). The origin of the Ivrea–Verbano basic formation (western Italian Alps); whole rock geochemistry. *Bollettino della Societa Geologica Italiana* **94**, 1149–1186.

Rivalenti, G., Rossi, A., Franca, S. & Sinigoi, S. (1984). The layered series of the Ivrea–Verbano igneous complex, Western Alps, Italy. *Tschermak's Mineralogische und Petrographische Mitteilungen* **33**, 77–99.

Roedder, P. L. & Emslie, R. F. (1970). Olivine–liquid equilibrium. *Contributions to Mineralogy and Petrology* **29**, 275–289.

Sisson, T. W. & Grove, T. L. (1992). Experimental investigations of the role of H_2O in calc-alkaline differentiation and subduction zone magmatism. *Contributions to Mineralogy and Petrology* **113**, 143–166.

Thompson, R. N. (1974). Primary basalts and magma genesis. I. Skye, North-West Scotland. *Contributions to Mineralogy and Petrology* **45**, 317–341.

Thompson, R. N. (1975*a*). Primary basalts and magma genesis. II. Snake River Plain, Idaho, U.S.A. *Contributions to Mineralogy and Petrology* **52**, 213–232.

Thompson, R. N. (1975*b*). The 1-atmosphere liquidus oxygen fugacities of some tholeiitic intermediate, alkalic and ultra alkalic lavas. *American Journal of Science* **275**, 1049–1072.

Ulmer, P. (1989). The dependence of the Fe^{2+}–Mg cation-partitioning between olivine and basaltic liquid on pressure, temperature and composition. An experimental study to 30 kbars. *Contributions to Mineralogy and Petrology* **101**, 261–273.

Ulmer, P. & Luth, R. W. (1991). The graphite–COH fluid equilibrium in P, T, fO_2 space. An experimental determination to 30 kbar and 1600°C. *Contributions to Mineralogy and Petrology* **106**, 265–272.

Wager, L. R. (1960). The major element variation of the layered series of the Skaergaard intrusion (Greenland) and a re-estimation of the average composition of the hidden layered series and of the successive residual magmas. *Journal of Petrology* **1**, 364–398.

Yang, H. J., Kinzler, R. J. & Grove, T. L. (1996). Experiments and models of anhydrous, basaltic olivine–plagioclase–augite saturated melts from 0·001 to 10 kbar. *Contributions to Mineralogy and Petrology* **124**, 1–18.

Yoder, H. S. (1969). Calcalkalic andesites: experimental data bearing on the origin of their assumed characteristics. In: McBirney, A. R. (ed.) *Proceedings of the Andesite Conference. Department of Geology and Mineral Industries* **65**, 77–89.

Yoder, H. S. & Tilley, C. E. (1962). Origin of basalt magmas: an experimental study of natural and synthetic rock systems. *Journal of Petrology* **3**, 342–532.